

## Hadronic Collisions: A Quarkonium Factory

R. Baier

Fakultät für Physik, Universität Bielefeld, D-4800 Bielefeld 1, Federal Republic of Germany

R. Rückl

Sektion Physik, Universität München, D-8000 München 2, Federal Republic of Germany

Received 17 March 1983

**Abstract.** Hadronic collisions are quite efficient in producing new quark flavours due to the large gluon content of ordinary hadrons. In particular, one may expect sizable yields of heavy quark-antiquark bound states with various spin and orbital quantum numbers. Using perturbative QCD in combination with the nonrelativistic quarkonium model we present a fairly complete and detailed picture of charmonium and bottomonium production. We compare our results on inclusive  $J/\psi$  and  $\Upsilon$  distributions with high energy  $pp$  data and make predictions on  $\eta_c$  and  $\chi$  production.

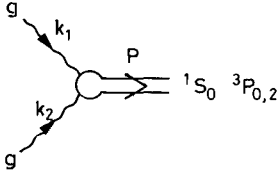
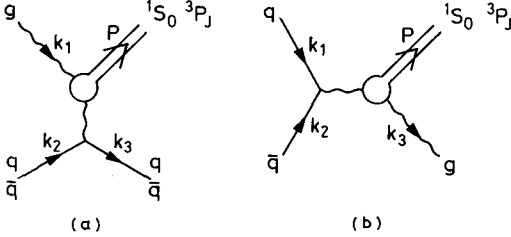
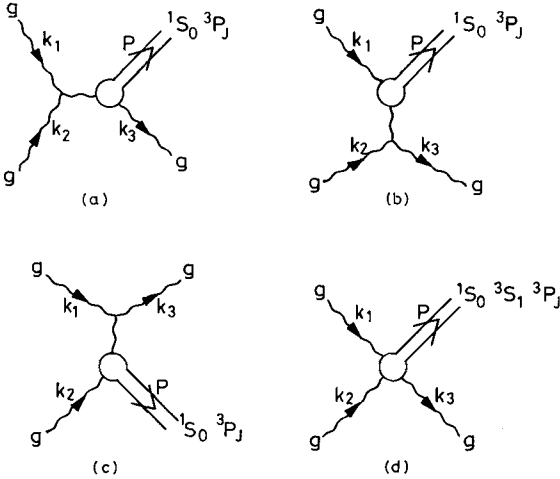
### I. Introduction

New flavour production is presently an active field of research [1]. The prospect of learning about the spectrum of fundamental constituents and their dynamics certainly justifies the considerable effort being made. A particular subject in this field which is receiving continuous attention is the production of heavy quark-antiquark resonances in hadronic collisions [2]. The latter have the advantage of yielding large rates and allowing for direct production of states with different spin ( $S$ ) and orbital ( $L$ ) quantum numbers as opposed to  $e^+e^-$ -annihilation where, in the dominant one-photon channel, only states with  $J=1$ ,  $C=P=-1$  can be reached directly. In this paper we give a detailed account of hadronic charmonium and bottomonium production in the framework of perturbative QCD and the nonrelativistic potential model for heavy quark-antiquark bound states. We evaluate, in particular, the inclusive  $p_T$

distributions of  $J/\psi$  and  $\Upsilon$  and compare our results with  $pp$  data at FNAL/ISR energies. The agreement is quite satisfactory and lends support to the dynamical assumptions made. We also present predictions on  $\eta_c$  and  $\chi$  production and give a brief outlook of detecting these states in future experiments.

Qualitatively, the theoretical picture adopted in this paper is rather simple. It is proposed that quarks carrying a new flavour quantum number  $Q$  are pairproduced in hard scattering processes between the light quark and gluon constituents of the colliding hadrons. These heavy  $Q\bar{Q}$ -pairs eventually form bound states with a probability determined by the appropriate quarkonium wave functions. Further, it is argued that, for sufficiently heavy quarks and for large transverse momenta, soft gluon as well as other nonperturbative effects such as higher twist contributions become negligible. If this is correct, as we assume, quarkonium production can be calculated in QCD perturbation theory. Figures 1–3 illustrate the lowest order processes we are concerned with in this paper. There is, obviously, a close relationship between some of these processes and the hadronic decay processes of quarkonia such as  $\eta_c$  or  $\chi_{0,2} \rightarrow 2g$  and  $J/\psi \rightarrow 3g$ . In fact, the two calculations are very similar [3, 4] as far as the general procedure is concerned. However, in case of quarkonium production the QCD cross sections have, finally, to be converted into observable hadronic cross sections employing the usual parton model formalism which involves the quark and gluon structure of the colliding hadrons.

The model outlined above has been applied to various aspects of hadronic production of heavy re-

Fig. 1. Quarkonium production to  $O(\alpha_s^2)$ Fig. 2. Quarkonium production to  $O(\alpha_s^3)$ : a  $g q$  or  $g \bar{q}$ -scattering, b  $q \bar{q}$ -annihilationFig. 3a-d. Quarkonium production to  $O(\alpha_s^3)$ : g-g-scattering

sonances [3] as well as, in an appropriately adjusted version, to lepton production [2]. In earlier investigations [3, 8] we have found consistency with FNAL and ISR data on  $J/\psi$  and  $\Upsilon$  production in  $pp$  collisions at large  $p_T$  [6, 7] and also with the latest EMC data on  $J/\psi$  muon production [9] in the inelastic region where the diffractive component is absent. These previous successes suggest a more detailed and complete exploitation of the model. That together with a description of the calculational techniques and a summary of the basic QCD cross sections is the main purpose of the present paper. Since the nucleon structure functions are best known we concentrate in our numerical analysis exclusively on  $pp$  collisions. The results, however, apply also to  $\bar{p}p$  collisions and can easily be generalized to other beam types.

The paper is organized as follows: In Chap. II we sketch the derivation of the perturbative QCD cross sections for the  $O(\alpha_s^2)$  and  $O(\alpha_s^3)$  processes exemplified in Figs. 1–3. The production pattern which emerges at the subprocess level is discussed quantitatively in Chap. III. Chapter IV describes how one converts the QCD cross sections to actual inclusive distributions in the frame work of the parton model. In Chap. V we, then, investigate the general pattern of large  $p_T$  charmonium and bottomonium production. This discussion is followed in Chap. VI by a detailed comparison of the invariant  $J/\psi$  and  $\Upsilon$  cross sections with experiment and by predictions on  $\eta_c$  and  $\chi$  production. Chapter VII, finally, summarizes the main results. There are also two Appendices, one (A) containing the basic QCD cross sections, the other (B) providing a complete list of our numerical input.

## II. QCD Cross Sections

In this chapter we describe the derivation of the lowest order QCD cross sections for quarkonium production initiated by gluons and light quarks. To  $O(\alpha_s^2)$ , one only has the gluon fusion process depicted in Fig. 1. This mechanism evidently populates the low  $p_T$  region with a mean  $p_T$  determined by the primordial transverse motion of the gluon constituents. Higher order contributions to the low  $p_T$  resonance production, such as  $q\bar{q} \rightarrow {}^{2S+1}L_J$  via two or three intermediate gluons\*, are not important at energies,  $\sqrt{s} \gtrsim 30$  GeV. Such processes, however, may play a significant role at lower energies, in particular for beams which contain valence anti-quarks. At the  $O(\alpha_s^3)$  level, in contrast, one has far more contributions. Most important are the two-by-two scattering processes shown in Figs. 2 and 3. Here, a gluon or ordinary quark recoils against the heavy resonance, thus leading to large transverse momenta. To  $O(\alpha_s^3)$ , there are also virtual contributions to the second order process of Fig. 1. Unfortunately, these corrections have not been calculated yet and are, therefore, not included in the present analysis. Note that in Figs. 1–3 we have omitted all diagrams which differ from the ones shown only by a permutation of the gluon lines.

The Feynman graphs introduced above exhibit two interesting facts: the sensitivity of the large  $p_T$  production to the three gluon vertex and the crucial role played by the quarkonium wave functions. Depending on the bound state quantum numbers there is a minimum number of gluons which must be coupled to a particular state in a given subprocess.

\* See, for example, the discussion of  $q\bar{q} \rightarrow {}^3P_J$  by Kühn [3]

This leads to the characteristic production pattern indicated in Figs. 1–3. On the one hand, this pattern, if observed, would be a rather convincing evidence for our assumption that the bound states are formed at short distances. On the other hand, one should be aware of the possibility that higher order corrections could wash out this striking pattern, at least to some extent.

### 1. Matrix Elements – General Formalism

The amplitudes for the processes shown in Figs. 1–3 can be written in the form\*

$$A(P) = \int \frac{d^4 q}{(2\pi)^4} \text{Tr} [O(P, q) \phi(P, q)] \quad (1)$$

where  $\phi(P, q)$  is the Bethe-Salpeter wave function of the bound state produced and  $O(P, q)$  is derived from the perturbative part of the diagrams with the heavy quark legs cut off. The heavy quark spinors,  $u(\frac{1}{2}P + q, s)$  and  $\bar{v}(\frac{1}{2}P - q, \bar{s})$  are included in  $\phi$ . In the above,  $P$  is the bound state 4-momentum,  $2q$  is the relative momentum of the heavy quarks and  $s(\bar{s})$  denote their spins. For simplicity, we have suppressed the dependence of (1) on the momenta\*\*  $k_i$ ,  $i = 1, 2, 3$  of the light quarks and gluons involved.

As usual we assume that quarkonia are nonrelativistic bound states. In the restsystem of such a state, the relative momentum  $|\mathbf{q}|$  is small with respect to the quark mass  $m_Q$ . As a consequence, one can decompose the wave function of a state with spin  $S$ , orbital angular momentum  $L$  and total angular momentum  $J$  as follows:

$$\phi(P, q) = 2\pi \delta\left(q^0 - \frac{|\mathbf{q}|^2}{2m_Q}\right) \sum_{L_z, S_z} \psi_{LL_z}(\mathbf{q}) \langle LL_z; SS_z | JJ_z \rangle P_{SS_z}(P, q). \quad (2)$$

Here,

$$P_{SS_z}(P, q) = \sum_{s, \bar{s}} \langle \frac{1}{2}s; \frac{1}{2}\bar{s} | SS_z \rangle u(\frac{1}{2}P + q, s) \bar{v}(\frac{1}{2}P - q, \bar{s}), \quad (3)$$

plays a role of a spin projection operator and  $\psi_{LL_z}(\mathbf{q})$  is the nonrelativistic bound state wave function. The brackets are usual Clebsch-Gordon coefficients. Substitution of (2) into (1) yields:

$$A(P) = \sum_{L_z, S_z} \int \frac{d^3 q}{(2\pi)^3} \psi_{LL_z}(\mathbf{q}) \langle LL_z; SS_z | JJ_z \rangle \cdot \text{Tr} [O(P, q) P_{SS_z}(P, q)]. \quad (4)$$

\* Here, we follow the notation of Guberina et al. [10]

\*\* The momentum assignment can be read off from Figs. 1–3

Since, the wave function,  $\psi_{LL_z}(\mathbf{q})$ , damps out contributions from integration regions where  $|\mathbf{q}| \sim O(m_Q)$  it is appropriate to expand (4) in powers of  $|\mathbf{q}|$  and to retain only the first nonvanishing terms of this expansion. This results in the following simple formula for  $S$ -waves ( $L=0, J=S$ ):

$$A(P) = \frac{1}{\sqrt{4\pi}} R_0 \text{Tr} [O(P, 0) P_{SS_z}(P, 0)]. \quad (5)$$

The parameter,

$$\frac{1}{\sqrt{4\pi}} R_0 = \int \frac{d^3 q}{(2\pi)^3} \psi_{00}(\mathbf{q}), \quad (6)$$

is essentially the value of the radial  $S$ -wave function at the origin. For  $P$ -waves ( $L=1, J=0, 1, 2$ ) one has to go one step further in the expansion of (4) because the  $P$ -wave function vanishes at the origin. From the term  $\sim q^\alpha$  one obtains:

$$A(P) = -i \sqrt{\frac{3}{4\pi}} R'_1 \sum_{L_z, S_z} \langle 1L_z; SS_z | JJ_z \rangle \varepsilon^\alpha(L_z) \frac{\partial}{\partial q_\alpha} \cdot \text{Tr} [O(P, q) P_{SS_z}(P, q)]|_{q=0}, \quad (7)$$

where  $R'_1$  is related to the integral,

$$\int \frac{d^3 q}{(2\pi)^3} q^\alpha \psi_{1L_z}(\mathbf{q}) = -i \varepsilon^\alpha(L_z) \sqrt{\frac{3}{4\pi}} R'_1(0), \quad (8)$$

and parameterizes, therefore, the derivative of the  $P$ -wave function at the origin. The polarization vector  $\varepsilon^\alpha(L_z)$  in (7) and (8) refers to a  $L=1$  system.

Finally, we have to specify the spin projection operators  $P_{SS_z}$  defined in (3). Up to irrelevant terms of  $O(|\mathbf{q}|^2)$  these matrices can be represented in a covariant form:

$$P_{SS_z} = \sqrt{\frac{1}{8m_Q^3}} \left[ \gamma \cdot \left( \frac{P}{2} + q \right) + m_Q \right] \Pi_{SS_z} \left[ -\gamma \cdot \left( \frac{P}{2} - q \right) + m_Q \right] \quad (9)$$

with

$$\Pi_{SS_z} = \begin{cases} \gamma_5 & \text{for } S=0 \\ \gamma \cdot \varepsilon(S_z) & \text{for } S=1 \end{cases} \quad (10)$$

for singlet ( $S=0$ ) and triplet ( $S=1$ ) states, respectively.

The formalism sketched above is worked out in detail and in a quite general form in [11]. We have made extensively use of this preparatory work in deriving the matrix elements for all processes\* con-

\* As mentioned earlier, some of these processes have already been studied in the literature [3, 4]. Our  $O(\alpha_s^3)$  results on  $^1S_0$  and  $^3P_J$  production, however, are novel

sidered in this paper. Here, it may suffice to discuss one specific example which is also of particular phenomenological interest.

## 2. $\eta_c$ Production in $O(\alpha_s^3)$ – a Specific Example

From (5), (9) and (10) one obtains (11) for the amplitude of a singlet  $S$ -wave such as the  $\eta_c$  the formal expression:

$$A = \frac{1}{\sqrt{16\pi M}} R_0 \text{Tr}[O(P, 0)(\not{P} + M)\gamma_5]. \quad (11)$$

Here, we have set the resonance mass  $M = 2m_Q$ , an approximation which is perfectly consistent with the nonrelativistic nature of the quarkonium. Starting with the simplest  $O(\alpha_s^3)$  subprocess,  $gq \rightarrow {}^1S_0 q$ , we find from the Feynman graphs illustrated in Fig. 2a the matrix:

$$O^a(P, 0) = g_s^3 \frac{\lambda^a}{4\sqrt{3}} \cdot \frac{\not{\epsilon}_1(\not{P} - 2\not{k}_1 + M)\gamma^\mu + \gamma^\mu(2\not{k}_1 - \not{P} + M)\not{\epsilon}_1}{\hat{t}(\hat{t} - M^2)} \cdot \bar{u}(k_3, s_3)\gamma_\mu u(k_2, s_2). \quad (12)$$

Then, upon substitution of (12) in (11) and some algebraic manipulations, one derives:

$$A^a(gq \rightarrow {}^1S_0 q) = \frac{g_s^3 R_0 \lambda^a}{\sqrt{3\pi M}(-\hat{t})(\hat{t} - M^2)} \varepsilon^{\mu\nu\rho\sigma} \varepsilon_{1\nu} \cdot k_{1\rho}(k_2 - k_3)_\sigma \bar{u}(k_3, s_3)\gamma_\mu u(k_2, s_2). \quad (13)$$

Here,  $\lambda^a$  are the usual  $SU(3)$ -colour matrices normalized according to  $\text{Tr}(\lambda^a \lambda^b) = 2\delta^{ab}$  and  $\varepsilon_1$  denotes the polarization vector of the initial gluon. The invariant variables  $\hat{s}$ ,  $\hat{t}$  and  $\hat{u}$  are defined in the Appendix A. The amplitude of the subprocess,  $q\bar{q} \rightarrow {}^1S_0 g$ , can be inferred from (13) simply by a change of momenta,  $k_1 \leftrightarrow -k_3$ , as it is obvious from Fig. 2b.

Finally, the matrix element of the process,  $gg \rightarrow {}^1S_0 g$ , is given by the coherent sum:

$$A(gg \rightarrow {}^1S_0 g) = A_s + A_i + A_u + A_D. \quad (14)$$

This first three contributions come from the  $\hat{s}$ ,  $\hat{t}$  and  $\hat{u}$ -channel gluon exchange graphs shown in Figs. 3a–c, respectively, whereas the last amplitude refers to the diagram\*, Fig. 3d. Starting with diagram, Fig. 3a, one finds:

$$O^{abc}(P, 0) = g_s^3 \frac{f^{abc}}{2\sqrt{3}} \cdot \frac{-\not{\epsilon}_3(\not{P} + 2\not{k}_3 - M)\gamma^\sigma + \gamma^\sigma(\not{P} + 2\not{k}_3 + M)\not{\epsilon}_3}{\hat{s}(\hat{s} - M^2)} \cdot \varepsilon_1^\mu \varepsilon_2^\nu C_{\mu\nu\sigma}(k_1, k_2). \quad (15)$$

where the tensor  $C_{\mu\nu\sigma}(k_1, k_2) = g_{\mu\nu}(k_2 - k_1)_\sigma - g_{\nu\sigma}(k_1 + 2k_2)_\mu + g_{\mu\sigma}(2k_1 + k_2)_\nu$  describes the three-gluon vertex and the  $\varepsilon_i$ 's are the gluon polarization vectors. The colour structure is characterized by the antisymmetric  $SU(3)$  structure constants,  $f^{abc}$ . Substitution of (15) in (11) gives, then:

$$A_s^{abc} = \frac{2g_s^3 R_0 f^{abc}}{\sqrt{3\pi M} \hat{s}(\hat{s} - M^2)} \varepsilon_1^\mu \varepsilon_2^\nu C_{\mu\nu\sigma}(k_1, k_2) \varepsilon^{\sigma\rho\tau\lambda} \cdot \varepsilon_{3\rho}(k_1 + k_2)_\tau k_{3\lambda}. \quad (16)$$

The amplitudes,  $A_i$  and  $A_u$ , follow trivially from (16) through the crossing relations:

$$A_i^{abc} = A_s^{cba}(k_1 \leftrightarrow -k_3, \varepsilon_1 \leftrightarrow \varepsilon_3) \quad (17)$$

and

$$A_u^{abc} = A_s^{acb}(k_2 \leftrightarrow -k_3, \varepsilon_2 \leftrightarrow \varepsilon_3). \quad (18)$$

The remaining amplitude  $A_D$  shows a different and more complex structure. Explicitly, one has:

$$A_D^{abc} = -\frac{g_s^3 R_0 f^{abc}}{\sqrt{12\pi M}} \text{Tr} \left\{ \left[ \frac{(\varepsilon_1 \cdot P + \not{k}_1 \not{\epsilon}_1) \not{\epsilon}_2 (\varepsilon_3 \cdot P - \not{k}_3 \not{\epsilon}_3)}{(\hat{s} - M^2)(\hat{t} - M^2)} + \frac{(\varepsilon_3 \cdot P - \not{k}_3 \not{\epsilon}_3) \not{\epsilon}_1 (\varepsilon_2 \cdot P + \not{k}_2 \not{\epsilon}_2)}{(\hat{s} - M^2)(\hat{u} - M^2)} + \frac{(\varepsilon_2 \cdot P + \not{k}_2 \not{\epsilon}_2) \not{\epsilon}_3 (\varepsilon_1 \cdot P + \not{k}_1 \not{\epsilon}_1)}{(\hat{t} - M^2)(\hat{u} - M^2)} \right] (\not{P} + M) \gamma_5 \right\}. \quad (19)$$

Here, the first bracket in the trace is essentially the matrix  $O(P, 0)$ . The trace itself was evaluated further on the computer. This technical remark may conclude our illustrative detour.

## 3. Cross Sections

Having explained how one obtains the amplitudes it is, now, straight forward to calculate the cross sections. Formally, the  $O(\alpha_s^2)$  gluon fusion cross sections are given by

$$\sigma(gg \rightarrow {}^{2S+1}L_J) = \frac{\pi}{\hat{s}^2} \bar{\Sigma} |A(gg \rightarrow {}^{2S+1}L_J)|^2 \delta\left(1 - \frac{M^2}{\hat{s}}\right), \quad (20)$$

whereas the differential cross sections of the  $O(\alpha_s^3)$  scattering processes follow from the relation:

$$\frac{d\sigma}{d\hat{t}}(ab \rightarrow {}^{2S+1}L_J c) = \frac{1}{16\pi\hat{s}^2} \bar{\Sigma} |A(ab \rightarrow {}^{2S+1}L_J c)|^2. \quad (21)$$

\* This mechanism is the only one which yields directly produced  $J/\psi$ 's and  $\Upsilon$ 's at large  $p_T$

The sum,  $\bar{\Sigma}$ , in (20) and (21) includes spin and colour summation as well as appropriate averaging. The final analytic results are summarized in Appendix A. Below we make a few comments.

Due to the presence of the three-gluon vertex in the  $O(\alpha_s^3)$  processes,  $gg \rightarrow {}^1S_0 g$  and  $gg \rightarrow {}^3P_J g$ , one has, in general, also ghost contributions to these cross sections. It is possible to avoid these unphysical modes by choosing a planar gauge which involves an extra gauge vector  $n$  with the properties  $n^2 = 1$  and  $n \cdot \varepsilon_i = 0$ . The price one must pay is a complication in the algebra because of the awkward polarization sum<sup>\*</sup>:

$$\Sigma \varepsilon_{i\mu} \varepsilon_{iv} = -g_{\mu\nu} + \frac{k_{i\mu} n_\nu + k_{i\nu} n_\mu}{k_i \cdot n} - \frac{k_{i\mu} k_{i\nu}}{(k_i \cdot n)^2}. \quad (22)$$

The large number of diagrams which contribute to these particular cross sections makes the calculation even more time consuming. We have, therefore, evaluated the above cross sections on the computer with the aid of the algebraic program SCHOONSHIP [12]. Gauge invariance and the singularities at  $\hat{t} \rightarrow 0$  have, then, be used to check the results.

This brings up another problem, namely the fact that the cross sections,  $\frac{d\sigma}{d\hat{t}}(gq \rightarrow ({}^1S_0, {}^3P_{0,2})q)$  and  $\frac{d\sigma}{d\hat{t}}(gg \rightarrow ({}^1S_0, {}^3P_{0,2})g)$ , are divergent as  $\hat{t} \rightarrow 0$  (see e.g. (A7), (A8), (A10) and (A13)). The physical solution of this problem would be to factorize out and absorb these initial state singularities into the distribution functions of the gluons involved in the  $O(\alpha_s^2)$  subprocess  $gg \rightarrow ({}^1S_0, {}^3P_{0,2})$ , rendering these structure functions scale dependent as dictated by the QCD evolution equations [13]. To demonstrate how this comes about let us consider the  ${}^1S_0$  cross sections given in (A7) and (A13). Integrating over  $\hat{t}$  and keeping only the leading logarithmic term, gives

$$\int d\hat{t} \frac{d\sigma}{d\hat{t}}(gq \rightarrow {}^1S_0 q) \rightarrow \sigma_0(gg \rightarrow {}^1S_0) \frac{\alpha_s}{2\pi} P_{q \rightarrow g} \left( \frac{M^2}{\hat{s}} \right) \ln \hat{t} \quad (23)$$

and, similarly,

$$\int d\hat{t} \frac{d\sigma}{d\hat{t}}(gg \rightarrow {}^1S_0 g) \rightarrow \sigma_0(gg \rightarrow {}^1S_0) \frac{\alpha_s}{2\pi} P_{g \rightarrow g} \left( \frac{M^2}{\hat{s}} \right) \ln \hat{t}. \quad (24)$$

In the above,  $\sigma_0$  is defined as the factor multiplying the  $\delta$ -function of the  $O(\alpha_s^2)$  cross section,  $\sigma(gg \rightarrow {}^1S_0)$ , given in (A4). The quantities

$$P_{q \rightarrow g}(\tau) = \frac{4}{3} \frac{1 + (1 - \tau)^2}{\tau}, \quad (25)$$

<sup>\*</sup> We choose  $n_\mu = P_\mu/M$

and

$$P_{g \rightarrow g}(\tau) = 6 \left( \frac{1 - \tau}{\tau} + \frac{\tau}{1 - \tau} + \tau(1 - \tau) \right), \quad \tau \neq 1, \quad (26)$$

are two of the well-known Altarelli-Parisi functions [13] which describe the probability for a quark and gluon, respectively, to radiate off a gluon with an energy fraction  $\tau$ . These functions generate scaling violations in the structure functions and lead to a QCD improved formulation of the parton model as discussed, for example in [14]. Relations similar to (23) and (24) can also be established for the corresponding  $P$ -wave cross sections.

In our numerical analysis we have actually chosen a more pragmatism regularization. We simply impose a cut off on the divergent  $p_T$  distributions at  $p_T \sim 2 \text{ GeV}/c$  and interpolate smoothly to the low  $p_T$  spectrum dominated by the  $O(\alpha_s^2)$  processes. This does not at all affect the large  $p_T$  results. The low  $p_T$  spectra, on the other hand, suffer anyway from uncertainties due to higher order loop corrections and primordial transverse motion. Thus, our low  $p_T$  results should only be considered as rough estimates. Nevertheless, they illustrate what one can expect within the model.

### III. The Production Pattern at the Subprocess Level

To understand how much of the pure perturbative QCD pattern is, at the end, observable in the inclusive distribution, it is useful to study the QCD cross sections in more detail before the parton model machinery is applied. For that purpose, we plot in Fig. 4 the  $O(\alpha_s^3)$  charmonium cross sections versus the scaled momentum transfer,  $-\hat{t}/\hat{s}$ , for a typical value of the subenergy,  $\hat{s} = x_1 x_2 s = 50 \text{ GeV}^2$ . At the highest ISR energy,  $\sqrt{s} = 63 \text{ GeV}$ , and for a symmetric parton configuration,  $x_1 = x_2$ , this corresponds to a typical mean momentum fraction,  $x \sim 0.1$ . The absolute normalization of the curves shown in Fig. 4 depends on three parameters, the QCD coupling constant,  $\alpha_s$ , and the  $S$ - and  $P$ -wave function parameters,  $R_0$  and  $R'_1$ . Numerically, we have used the values (B7)–(B9) given in Appendix B. <sup>\*</sup> It should be mentioned that the values of  $R_0$  are derived from the experimental values of the leptonic widths, (B4), using the lowest order relation (A2), while the values of  $R'_1$  are taken from a potential model analysis [15].

First, we observe from Fig. 4 that the gluon-gluon and the gluon-quark scattering processes give rise to very similar resonance cross sections, apart

<sup>\*</sup> A detailed discussion of our parametrization can be found in our earlier papers [3]

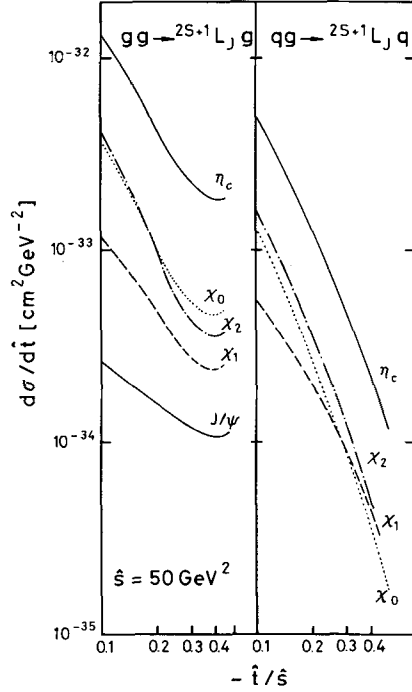


Fig. 4.  $O(\alpha_s^3)$ -QCD cross sections for charmonium production at a typical subenergy  $\sqrt{\hat{s}}$

from the special case of the  $J/\psi$  and other triplet  $S$ -waves which can only be produced via  $gg \rightarrow {}^3S_1 g$ . The apparent differences at large  $\hat{t}$  or, equivalently, at small  $\hat{u}$  are caused by the usual procedure to symmetrize the  $gq$  contributions with respect to  $\hat{t}$  and  $\hat{u}$  not until the structure function are folded in while the  $gg$  cross sections are symmetric to start with. The cross sections  $\frac{d\sigma}{dt̂}(q\bar{q} \rightarrow {}^{2S+1}L_J g)$  are not plotted in Fig. 4. These are in all cases of the order of  $10^{-35} \text{ cm}^2 \text{ GeV}^{-2}$  or smaller and, therefore, totally negligible in the energy range considered. As an important consequence, quarkonium production in  $pp$  and  $\bar{p}p$  collisions is expected to be practically identical at high energies.

The most interesting feature exhibited in Fig. 4, however, is the striking pattern in the relative abundancies of the various states. As already pointed out in Chap. II, this pattern is a direct consequence of our dynamical assumptions and, thus, a crucial prediction of the model. How the observed pattern emerges can best be seen by examining the large  $\hat{t} \simeq \hat{u}$  region\*. Considering the quark-gluon processes, for example, one finds from (A7) and (A8),

$$\frac{d\sigma}{dt̂}({}^3P_0) : \frac{d\sigma}{dt̂}({}^1S_0) \sim 4 \frac{R_1'^2/M^2}{R_0^2}. \quad (27)$$

\* For the following analysis one may neglect the mass differences within one system

The popular potential models, typically, give a rather small number for the above ratio. Using our favoured parameters, (B7) and (B8), one obtains, in particular,

$$\frac{R_1'^2/M^2}{R_0^2} \simeq \begin{cases} 2 \times 10^{-2} & \text{for charmonium} \\ 3 \times 10^{-3} & \text{for bottomonium.} \end{cases} \quad (28)$$

This explains the dominance of  $\eta_c$  production illustrated by Fig. 4. The  $P$ -wave states, on the other hand, are produced at large  $\hat{t}$  in fixed proportions. Focussing again on the  $qg$  processes,

$$\frac{d\sigma}{dt̂}({}^3P_0) : \frac{d\sigma}{dt̂}({}^3P_1) : \frac{d\sigma}{dt̂}({}^3P_2) \sim 1:6:2 \quad (29)$$

as can be easily derived from (A8)–(A10).

The crucial dynamical role played by the bound state quantum number is nicely demonstrated by the ratio of  $\eta_c$  to  $J/\psi$  production. Here, the wave functions are roughly the same, since both states are  $S$ -waves. Thus the more than an order of magnitude difference of the  $\eta_c$  and  $J/\psi$  cross sections exhibited in Fig. 4 must be due to the different effective coupling (10) of a  $S=0$  state compared to a  $S=1$  state. Indeed, one can show from (A12) and (A13) that at large  $\hat{t} \simeq \hat{u}$

$$\frac{d\sigma}{dt̂}({}^1S_0) : \frac{d\sigma}{dt̂}({}^3S_1) \sim 2 \frac{\hat{s}}{M^2}. \quad (30)$$

This quantifies the above statement and proves that  $J/\psi$  production is highly suppressed with respect to  $\eta_c$  production due to the different spin structure.

Similarly, one can analyse the pattern at small  $\hat{t}$  in Fig. 4. However, this exercise is a little more difficult because of the divergencies of some of the cross sections as  $\hat{t} \rightarrow 0$ . We should also note that the above cross section ratios, (27), (29) and (30), are valid asymptotically, i.e. for large values of  $\hat{s}/M^2$ . This is the reason why, for example, the ratios (29) differ from what one actually observes in Fig. 4 where  $\hat{s}/M^2 \sim 5$ . Everything we said above applies to the bottomonium cross sections as well except that the asymptotic region is shifted to much higher energies because of the larger bound state mass,  $M \sim 10 \text{ GeV}$ .

#### IV. Parton Model Formalism and Inclusive Distributions

The link between the quark-gluon dynamics and the real hadronic world is provided by the parton model. Roughly speaking, the hadrons are replaced by their quark and gluon constituents and the actual hadronic cross sections are represented as convo-

lutions of the short-distance QCD cross sections and the momentum distributions of these constituents.

### 1. Hard Scattering Formulas

Below we provide the hard scattering formulas which, eventually, lead to the inclusive resonance cross sections in the framework of the parton model. For the  $O(\alpha_s^2)$  gluon fusion processes, one has

$$E \frac{d^3\sigma}{d^3p} ({}^{2S+1}L_J) = \frac{1}{\pi} G_g(x_1) G_g(x_2) \cdot \sigma_0(gg \rightarrow {}^{2S+1}L_J) \delta(p_T^2). \quad (31)$$

The index  $a$  distinguishes the structure function,  $G_a(x)$ , with respect to the various parton species, while  $x$  is defined as the momentum fraction of the hadron carried by a particular parton. These fractions are constraint in (31), kinematically, to wit

$$x_1 = \frac{1}{2} \left( x_F + \sqrt{x_F^2 + \frac{4M^2}{s}} \right) \\ x_2 = \frac{M^2}{sx_1} \quad (32)$$

where  $x_F = 2p_L/\sqrt{s}$ . The short-distance cross sections  $\sigma_0(gg \rightarrow {}^{2S+1}L_J)$  involved in (31) have been defined in connection with (23) and (24), and can be obtained from (A4)–(A6). For the  $O(\alpha_s^3)$  cross sections, (A7)–(A13), the appropriate convolution formula reads as follows:

$$E \frac{d^3\sigma}{d^3p} ({}^{2S+1}L_J) = \sum_{a,b} \int dx_a dx_b G_a(x_a) G_b(x_b) \frac{\hat{s}}{\pi} \frac{d\sigma}{d\hat{t}} \cdot (ab \rightarrow {}^{2S+1}L_J c) \otimes \delta(\hat{s} + \hat{t} + \hat{u} - M^2). \quad (33)$$

Here, one sums over all constituents of the colliding hadrons which participate in the hard scattering processes shown in Figs. 2 and 3. Further, it proves convenient to express the invariants  $\hat{s}$ ,  $\hat{t}$  and  $\hat{u}$  defined in (A1) in terms of the rapidity,  $y$ , and transverse momentum,  $p_T$ , of the resonance, that is

$$\hat{s} = x_a x_b s \\ \hat{t} = -x_a \sqrt{s} \sqrt{M^2 + p_T^2} e^y + M^2 \\ \hat{u} = -x_b \sqrt{s} \sqrt{M^2 + p_T^2} e^{-y} + M^2. \quad (34)$$

Concentrating on  $pp$  collisions and working in lowest order perturbation theory we may simply use the quark and gluon structure functions measured in deep inelastic scattering. Whereas the quark distributions are quite well determined, the gluon structure function is still not too precisely known, at least not in the full  $Q^2$  range covered by our analysis.

Since, on the other hand, all cross sections of interest in the present paper depend on the gluon distribution, most of them even quadratically, the above uncertainties also affect our numerical results. Further ambiguities come from possible scaling violations in the structure functions,  $G_a(x, Q^2)$ , and also from the running coupling constant,  $\alpha_s(Q^2)$ , defined in (B9). Here, the problem is to determine the optimal scale  $Q^2$  which, in principle, requires higher order calculations. In order to mark out how significantly these uncertainties could affect our conclusions we use too quite different sets of structure functions. For definiteness, both choices are given explicitly in Appendix B. Set I, (B10), is a scaling parametrization [16] with the standard gluon distribution

$$xG_g(x) = 3(1-x)^5. \quad (35)$$

Set II, (B11), on the other hand, includes scaling violations in accordance with the leading log QCD evolution equations [17]. The input gluon distribution is given below for comparison with (35):

$$xG_g(x, Q^2 = 5 \text{ GeV}^2) \simeq 2(1-x)^{2.9}. \quad (36)$$

Concerning the scale  $Q^2$ , we set  $Q^2 = M^2 + p_T^2$  which we believe is a reasonable choice. Of course, together with set I we use a fixed value of the QCD coupling constant, to wit  $\alpha_s = \alpha_s(M^2)$ .

### 2. Primordial Transverse Motion

The issue of primordial transverse motion of the constituents inside a hadron has been discussed repeatedly in the literature. On the one hand, fermi motion may be very important phenomenologically, on the other hand, it is not totally clear how to incorporate this nonperturbative effect in the hard scattering formalism. For the case at hand, the large  $p_T$  cross sections should not be affected very significantly by this problem, whereas the low  $p_T$  spectra are expected to be extremely sensitive to primordial transverse momenta. The latter assertion is obvious since the dominant  $O(\alpha_s^2)$  processes lead to very narrow  $p_T$  distributions (see e.g. (31)).

It has become popular to simulate the effects of the fermi motion by smearing out the bare inclusive spectra,  $E_q \frac{d^3\sigma}{d^3q}$ , by a Gaussian primordial transverse momentum distribution,  $f(\mathbf{k}_T)$ . Then, the corrected distribution is given by

$$E \frac{d^3\sigma}{d^3p} = \int d^2q_T \left[ E_q \frac{d^3\sigma}{d^3q} \right] f((\mathbf{p}_T - \mathbf{q}_T)^2). \quad (37)$$

Numerically, we use the parametrization, (B12), which has also been used to describe the Drell-Yan pair production [18] without invoking soft gluons. In particular, for the low  $p_T$  cross sections one derives from (31) and (37) to a good approximation:

$$E \frac{d^3 \sigma}{d^3 p} ({}^{2S+1}L_J) \simeq G_g(x_1) G_g(x_2) \sigma_0(gg \rightarrow {}^{2S+1}L_J) \cdot f(\mathbf{p}_T^2). \quad (38)$$

This shows explicitly that the low  $p_T$  spectra cannot be predicted reliably since the problem of the fermi motion has not been solved. In contrast, at large  $p_T$  the primordial  $p_T$  effect is roughly a factor two for charmonium and about (20–30)% for bottomonium in the range of energies and transverse momenta studied, and, therefore, comparable to the uncertainties from the structure functions.

### 3. Decay Contributions

So far we have disregarded the possibility of producing a particular state via the production and subsequent decay of a heavier resonance. Such contributions are, indeed, negligible in most cases either because of low production rates and/or because of small branching ratios. However, there is one potentially important example, namely the production of  $P$ -waves followed by their radiative decay,  ${}^3P_J \rightarrow {}^3S_1 \gamma$ . In this case both the cross sections (see Fig. 4) and the branching ratios (see (B6)) are big. We include these contributions in our final  $J/\psi$  and  $Y$  results by folding the parental  $P$ -wave cross sections,  $E_q \frac{d^3 \sigma}{d^3 q}$ , with isotropic decay distributions

$$\frac{E}{\Gamma_{\text{tot}}({}^3P_J)} \frac{d\Gamma({}^3P_J \rightarrow {}^3S_1 \gamma)}{d^3 p} = \frac{M_p^2 B({}^3P_J \rightarrow {}^3S_1 \gamma)}{\pi(M_p^2 - M^2)} \cdot \delta(M_p^2 + M^2 - 2q \cdot p). \quad (39)$$

The quantitative significance of the  $P$ -wave contributions to  $J/\psi$  and  $Y$  production is discussed in Chap. VI.

## V. The Large Transverse Momentum Behaviour

After having described the calculation, including the various approximations involved, we are now ready to present some numerical results. In this chapter, we restrict our discussion to large  $p_T$  quarkonium production which is most suitable for application of QCD perturbation theory. For a critical appraisal of the model it is important that the input parameters are clearly specified. This is done in Appendix B.

### 1. Inclusive Distributions

Figures 5 and 6 show the transverse momentum distributions of the most prominent charmonium and bottomonium states calculated from the  $O(\alpha_s^3)$  processes of Figs. 2 and 3 using the scaling structure functions of set I, Appendix (B10). These results are raw distributions in the sense that primordial  $p_T$  effects as well as contributions from  $P$ -wave decays are not taken into account\*.

Comparing the relative production yields of the various states in Fig. 5 to the relative magnitudes of the corresponding QCD-cross sections plotted in Fig. 4 one observes a very similar pattern. Obviously, the quark and gluon distributions do not wash out significantly the underlying short distance structure discussed in Chap. III. For this reason and for the fortunate fact that cross section ratios are much less parameter dependent than absolute cross sections, an experimental examination of the relative production yields would help considerably to clarify the mechanism of heavy resonance production. Even an order of magnitude comparison would provide valuable information. Figures 5 and 6 show, furthermore, that the overall patterns of charmonium and bottomonium production are quite similar. The decrease of the  ${}^3P_J$  cross sections relative to the  ${}^1S_0$  and  ${}^3S_1$  cross sections in the bottomonium case as compared to charmonium case is mainly due to the decreasing value of the wave function ratio,  $R_1^2/M^2 R_0^2$ , quantified in (28). As an interesting consequence, one expects a strong  $\chi$ -component in the inclusive  $J/\chi$  yields in contrast to  $Y$  productions which, at large  $p_T$ , should not proceed significantly via  $P$ -wave production and subsequent decay. Also this prediction of the model does, in essence, not depend crucially on the details of our numerical input and, hence, can serve as another useful and decisive test. As far as the absolute magnitude of the cross sections exhibited in Figs. 5 and 6 are concerned, one of the most interesting results is the quite substantial  $\eta_c$  production. We return to the latter in the next chapter.

Contemplating, finally, the slopes of the large  $p_T$  distributions one makes, among others, two remarkable observations. First, the bottomonium spectra are considerably flatter than the charmonium distributions indicating a power behaviour in the transverse energy,  $\sqrt{M^2 + p_T^2}$ , rather than in the transverse momentum itself. Furthermore, asymptotically at  $p_T \gg M$ , one has

$$\frac{d\sigma({}^1S_0, {}^3P_J)}{d\sigma({}^3S_1)} \sim \frac{p_T^2}{M^2}. \quad (40)$$

\* Fully inclusive distributions which include all these effects are the subject of the next chapter



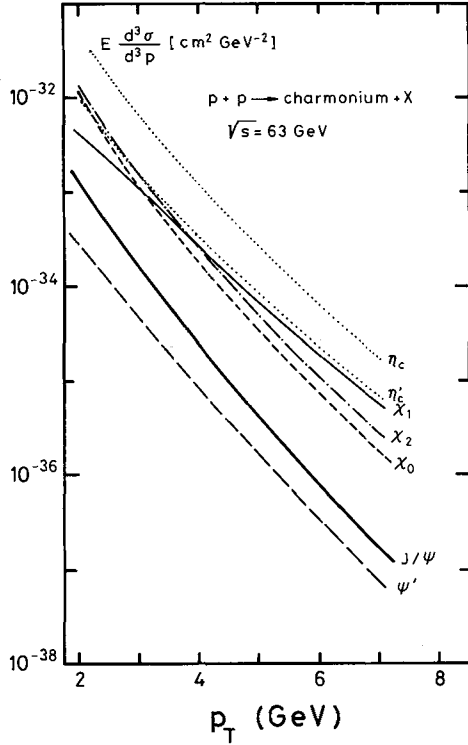


Fig. 5. Inclusive distributions of charmonium resonances at  $\theta_{cm} = 90^\circ$  calculated from the  $O(\alpha_s^3)$ -QCD subprocesses

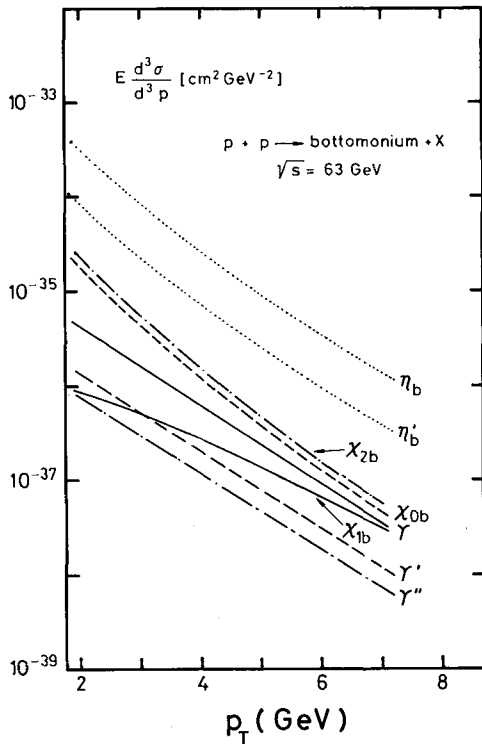


Fig. 6. Inclusive distributions of bottomonium resonances with similar specifications as in Fig. 5

These extra powers of  $p_T$  have the same origin\* as the factor  $\hat{s}/M^2$  pointed out in (30). The onset of the above asymptotic behaviour can already be seen in the charmonium cross sections of Fig. 5 whereas in the bottomonium case, Fig. 6, the transverse momenta considered are too small\*\* or, more precisely,  $p_T \lesssim M_Y$ .

## 2. Duality

Besides the model adopted in this paper there exists a different approach to heavy bound state production which makes use of the duality ideal [1] to estimate the resonance cross sections from the production cross sections of the corresponding unbound quark-antiquark pairs. More explicitly, one supposes the following relation:

$$\frac{d\sigma^{\text{RES}}}{d\xi} = \int_{2m_Q}^{2M_0} \frac{d\sigma^{Q\bar{Q}}}{dm d\xi} dm. \quad (41)$$

Here,  $d\xi$  is a given phase space element and  $m$  is the invariant mass of the unbound  $Q\bar{Q}$ -pair. The left-hand side of (41) involves a sum over all resonances with masses below the threshold,  $2M_0$ , for the production of mesons which carry the particular heavy flavour considered, openly. For charm,  $M_0$  is the mass of the highest  $D$  meson whereas for bottom,  $M_0 = M_B$ . The individual contribution of a particular state to the total resonance cross section in (41) is not known theoretically in the duality approach. Calculating the right-hand-side of (41) and comparing the result with the measured  $J/\psi$  cross section, one finds\*\*\* [19], phenomenologically, in  $pp$  collisions at  $\sqrt{s} \simeq 6$  to  $63$  GeV,

$$\frac{d\sigma}{dy}(J/\psi) \simeq \frac{1}{12} \int_{2m_c}^{2M_D} \frac{d\sigma^{c\bar{c}}}{dm dy} dm. \quad (42)$$

From the above and (41) one concludes that a fraction,  $F_{J/\psi} = \frac{1}{12}$ , of the charmonium cross section is due to  $J/\psi$  production. Analogously, the measured  $Y$  production amounts to a fraction  $F_Y = \frac{1}{90}$  of the bottomonium cross section calculated [19] according to (41). In our approach, on the contrary, the absolute normalizations are determined and the above fractions are predictable. Below, we estimate  $F_{J/\psi}$  and  $F_Y$

\* The assertion (40) follows directly from the QCD-cross sections (A7)–(A13) using the relation  $M^2 + p_T^2 = (\hat{t} - M^2)(\hat{u} - M^2)/\hat{s}$ , valid at  $\theta_{cm} = 90^\circ$ , and letting  $p_T$  become large, that is  $p_T \gg M$ .

\*\* The asymptotic behaviour shows up clearly for both, charmonium and bottomonium production, at  $\sqrt{s} = 540$  GeV and  $p_T > 10$  GeV/c as demonstrated in our analysis [3] of  $\bar{p}p$  production at ultra high energies.

\*\*\* The parameter used by the authors of [19] are very similar to ours.

and examine the duality relation (41) for large  $p_T$  production in the framework of our model.

To this end, we approximate the cross sections,  $E \frac{d\sigma^{\text{RES}}}{d^3p} \Big|_{y=0}$ , summed over all resonances with masses,  $M \leq 2M_D$  for charmonium and  $M \leq 2M_B$  for bottomonium, simply by adding up the inclusive distributions shown in Figs. 5 and 6, respectively. Defining the fractions,  $F_{2S+1L_J}$ , in analogy to (41) and (42) by  $E \frac{d^3\sigma}{d^3p}(^{2S+1}L_J) = F_{2S+1L_J} E \frac{d^3\sigma^{\text{RES}}}{d^3p}$ , one obtains at  $y=0$  and  $\sqrt{s}=63 \text{ GeV}$ :

$$F_{J/\psi} \sim \begin{cases} \frac{1}{70} & \text{at } p_T \sim 2 \text{ GeV}/c \\ \frac{1}{200} & \text{at } p_T \sim 7 \text{ GeV}/c \end{cases} \quad (43)$$

for directly produced  $J/\psi$ 's (process shown in Fig. 3d) and

$$F_{J/\psi} \sim \begin{cases} \frac{1}{30} & \text{at } p_T \sim 2 \text{ GeV}/c \\ \frac{1}{50} & \text{at } p_T \sim 7 \text{ GeV}/c \end{cases} \quad (44)$$

after including also the  $J/\psi$  yields from  $\chi$  production and decay. The latter mechanism is not important for  $Y$  production. Here, one has

$$F_Y \sim \begin{cases} \frac{1}{100} & \text{at } p_T \sim 2 \text{ GeV}/c \\ \frac{1}{50} & \text{at } p_T \sim 7 \text{ GeV}/c. \end{cases} \quad (45)$$

As the two main results of this exercise one sees that, in our model, the  $J/\psi$  and  $Y$  production is a fairly small fraction of the total charmonium and bottomonium production, respectively, and that these fractions are clearly not constant but depend on theonium type, the  $c\bar{m}$  energy and the kinematic region. Concerning the duality principle in the context of our model one can estimate the open  $c\bar{c}$  and  $b\bar{b}$  cross sections,  $E \frac{d\sigma^{Q\bar{Q}}}{d^3p}$ , integrated over the appropriate mass windows from a calculation\* by Kunszt et al. [20]. Comparing the result to the corresponding resonance cross sections, we find that duality in the form of (41) holds quite well within our model keeping in mind the uncertainties in some of the wave function parameters which determine the normalization of the resonance cross sections. Leaving aside the absolute magnitude, the  $p_T$ -dependence of the open flavour and resonance production defined above agrees perfectly.

## VI. Postdictions, Predictions and Experiments

As far as the hadronic production of  $J/\psi$  and  $Y$  is concerned there exists already plenty of data. Also

\* Note that the parameters used in [20] differ in some cases considerably from ours. In the above comparison we corrected partly for these differences

the charmonium  $P$ -wave states,  $\chi_J$ , have been observed, although with less statistics and larger experimental uncertainties. Furthermore, a number of experiments is proposed [21] to search for the  $\eta_c$  in hadronic collisions. In the following, we work out inclusive cross sections for the states mentioned above in the framework of our model. Starting from the raw  $O(\alpha_s^3)$  cross sections\* presented in the last chapter we add the contributions from the low  $p_T$   $O(\alpha_s^2)$  processes, Fig. 1 and (31), and take into account primordial transverse motion according to (37). In case of the  $J/\psi$  and the  $Y$  we, further, include the contributions from  $P$ -wave production and radiative decay,  $^3P_J \rightarrow ^3S_1 \gamma$ , as explained in IV.3. Finally, in order to demonstrate how much scaling violations could affect our results, all cross sections are recalculated using the structure function of set II, (B11), and the running coupling constant  $\alpha_s(Q^2)$ , (B9), with  $Q^2 = M^2 + p_T^2$ . The resulting phenomenological cross sections are compared to measurements of several experiments.

### 1. $J/\psi$ and $Y$ Production

Figures 7 and 8 summarize the theoretical  $J/\psi$  and  $Y$  cross sections at  $\theta_{\text{cm}}=90^\circ$  as a function of  $p_T$  in comparison with CERN-ISR\*\* [5, 7] and FNAL [6] measurements. One sees that the model agrees reasonably well with the data in the absolute magnitude of the cross sections as well as in the transverse momentum\*\*\* and energy dependence. In particular, the flattening of the  $p_T$  spectra with increasing quarkonium mass explained in V.1 matches nicely with what one observes. Remarkable is also the quite substantial effect of the scale dependence of the effective QCD coupling constant,  $\alpha_s(M^2)$ , which amounts up to a factor,  $(\alpha_s(M_\psi^2)/\alpha_s(M_Y^2))^3 \sim 4$ , at large  $p_T$ . Furthermore, it is obvious from the Feynman graphs of Fig. 1 that, to lowest order, one has dominantly  $P$ -wave production and subsequent decay. This mechanism also contributes more than 50% to large  $p_T$   $J/\psi$  production via the processes shown in Figs. 2 and 3, whereas the  $Y$ 's at large  $p_T$  are predicted to originate to about 80% in the direct process, Fig. 3d. The range enclosed by the dashed and full curves in Figs. 7 and 8 characterizes the size of scale violating effects. From the  $Y$  cross sections, in

\* As discussed in II.3., eventual divergencies as  $p_T \rightarrow 0$  are regulated by imposing a cutoff at  $p_T \sim 2 \text{ GeV}/c$

\*\* The data plots published originally in [7] are not correct. In Fig. 7 and 8 we show the correct data set communicated to us by Stumer [7]

\*\*\* Note that at  $p_T \lesssim 2 \text{ GeV}/c$  the shape of the curves is determined by the primordial  $p_T$  distribution, (B12). Only integrated cross sections are predictable from the low  $p_T$   $O(\alpha_s^2)$  processes, Fig. 1

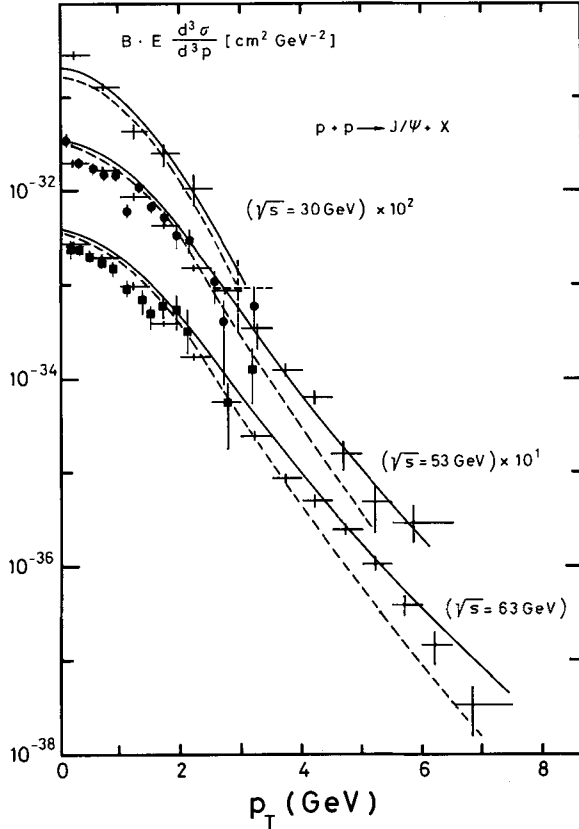


Fig. 7. Inclusive  $p_T$ -distributions of the  $J/\psi$  at  $\theta_{cm}=90^\circ$  and various energies. The full curves are scaling results, the dashed curves include scaling violations as described in the text. The data are taken from [5] ( $\bullet$  and  $\blacksquare$ ) and [7] (+)

particular, it becomes clear that consistency with experiment requires a relatively hard gluon distribution. A good description of the data is obtained in our model if one uses the standard form,  $xG_g(x) = 3(1-x)^5$ , assumed in set I, (B10), up to a scale as big as  $Q^2 \sim 100 \text{ GeV}^2$ .

Concerning the QCD scale  $\Lambda$  we remark that, numerically, a value of  $\Lambda \sim 500 \text{ MeV}$  is necessary to explain the observed  $J/\psi$  yields, in particular at large  $p_T$ . The  $O(\alpha_s^3)$  cross sections, for example, would decrease by a factor  $\sim 7$  if one takes  $\Lambda \sim 100 \text{ MeV}$ . Although there is no a priori problem in using a large effective QCD scale  $\Lambda$  in a lowest order calculation, there is a potential one. To settle this question one has to study higher orders of the perturbation expansion. In this context, it is very satisfactory that the model yields the correct size of the  $\Upsilon$  cross sections as illustrated in Fig. 8. Because of the large  $\Upsilon$  mass these results are much less sensitive to the actual value of  $\Lambda$  and, therefore, more reliable. Also the nonrelativistic approximation is expected to work better in the  $\Upsilon$  case.

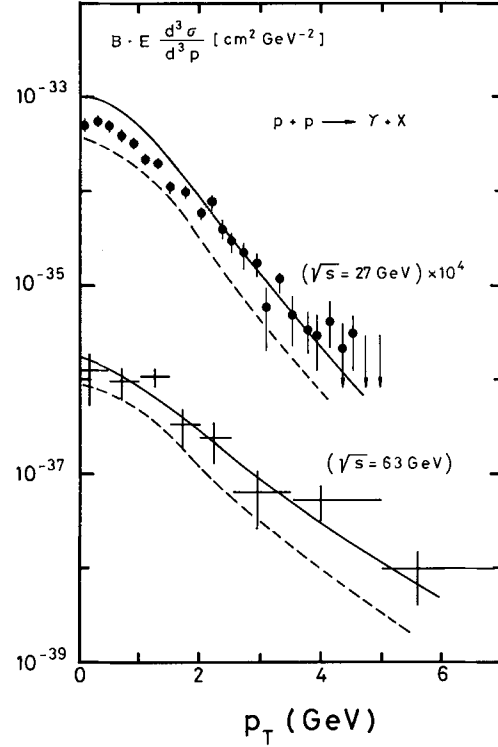


Fig. 8. Inclusive  $p_T$ -distributions of the  $\Upsilon$  at  $\theta_{cm}=90^\circ$  and two energies. The curves are as described in Fig. 7. The data are taken from [6] ( $\bullet$ ) and [7] (+)

Finally, we would like to address briefly the production of heavier  $^3S_1$  states such as  $\psi'$ ,  $\Upsilon'$  and  $\Upsilon''$ . Here, data are still sparse. Nevertheless, there seems to be agreement on a  $\psi'$  signal of the order of 1 to 2% in the dimuon channel in  $pp$  collisions [5, 22, 23]. Dividing out the leptonic branching ratios, (B5), this corresponds to the following cross section ratio at  $y=0$ :

$$\frac{d\sigma}{dy}(\psi') / \frac{d\sigma}{dy}(J/\psi) \sim (10 \text{ to } 16) \%. \quad (46)$$

The model, on the other hand, yields a ratio of about 20% from the direct source,  $gg \rightarrow ^3S_1 g$ , alone. The extra  $\chi$  contributions to  $J/\psi$  production should, then, lower this number in agreement with (46). Note that  $P$ -wave contributions to  $\psi'$  production are negligible since the  $\chi'$  resonances are lying above the open charm threshold and are, therefore, expected to have tiny branching ratios into the  $\psi'$ . For the heavier bottomonium  $S$ -wave states,  $\Upsilon'$  and  $\Upsilon''$ , we predict at  $y=0$  and ISR energies:

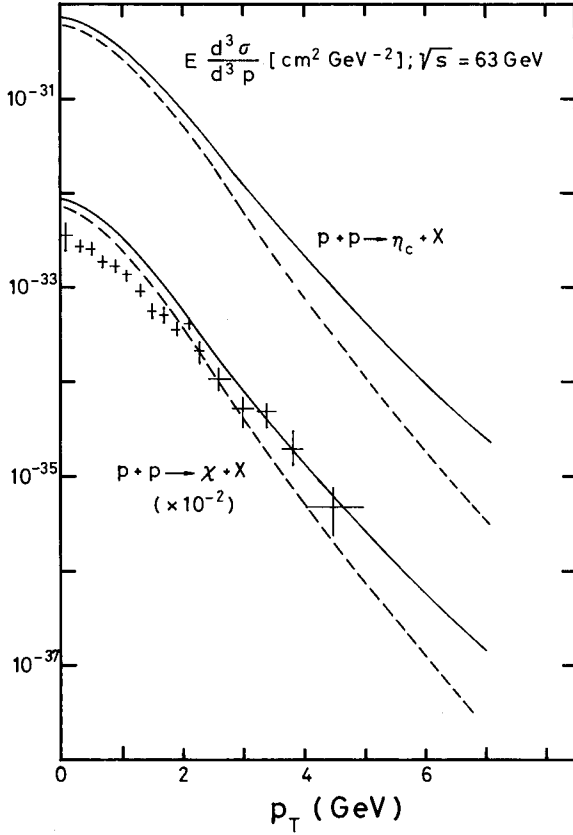


Fig. 9. Predicted  $\eta_c$ - and  $\chi$ -cross sections at  $\theta_{\text{cm}}=90^\circ$  for scaling structure functions (full curves) and including scale violations (dashed curves). The  $\chi$ -data are taken from [23]

$$\frac{d\sigma}{dy}(\gamma') \left/ \frac{d\sigma}{dy}(\gamma) \right. < 30\% \quad (47)$$

and

$$\frac{d\sigma}{dy}(\gamma'') \left/ \frac{d\sigma}{dy}(\gamma) \right. < 15\%. \quad (48)$$

The above upper limits are again ratios expected from the direct process alone. Experimentally, one finds [24]  $\gamma'/\gamma \sim (37 \pm 14)\% \times B_l(\gamma)/B_l(\gamma')$  and  $\gamma''/\gamma \sim (8 \pm 8)\% \times B_l(\gamma)/B_l(\gamma'')$  where  $B_l(^3S_1)$  denotes the relevant leptonic branching ratio. The large experimental uncertainties prevent a definite conclusion. Model and experiment certainly appear compatible.

## 2. $\chi$ and $\eta_c$ Production

The production of  $P$ -waves in hadronic collisions is, for various reasons, a particularly interesting process. Experimentally, such states should be accessible at the same level as  $S$ -waves in contrast to  $e^+e^-$ -annihilation where  $P$ -waves can only be produced

via decays of heavier  $^3S_1$ -states or in higher order processes such as 2-photon-scattering or 1-photon-production accompanied by hadronic jets. Theoretically,  $P$ -wave production can effectively be used to distinguish between various models of quarkonium production as pointed out in [25].

Figure 9 shows the fully inclusive  $\chi$  cross section summed over the three states with total angular momenta  $J=0, 1$  and 2. The theoretical prediction is obtained as outlined at the beginning of this chapter. The experimental cross section is published in [23] in arbitrary units. We have, therefore, normalized the data points in Fig. 9 to the absolutely normalized prediction at  $p_T \sim 2 \text{ GeV}/c$ . The large  $p_T$  spectrum is well described by the model whereas there is a slight discrepancy at  $p_T \lesssim 2 \text{ GeV}$ . This discrepancy, however, is not too significant since the shape at low  $p_T$  cannot be predicted reliably within the model as discussed in IV.2. On the contrary, the low  $p_T$  spectrum shown in Fig. 9 directly reflects the primordial transverse momentum distribution (B12) as pointed out in (38). Only the normalization is determined by the  $O(\alpha_s^2)$  cross sections (A5) and (A6). From Fig. 9 one finds for the integrated  $\chi$  cross section at  $y=0$ ,  $\frac{d\sigma}{dy}(\chi) \sim 2 \mu b$ . It should be noted, however, that this result depends on the  $P$ -wave function parameter,  $R'_1$ , the value (B8) of which we have taken from a potential model analysis [15]. Thus, the above number should be used with caution.

A cross section of similar magnitude is predicted by the model for the production of  $\eta_c$ , to wit\*  $\frac{d\sigma}{dy}(\eta_c) \sim 2 \mu b$  at  $y=0$ . Here, the absolute normalization depends on the  $S$ -wave function at the origin,  $R_0$ , which is relatively well known. Such big a cross section, of course, suggests to search for the  $\eta_c$  in hadronic collisions. In fact,  $\eta_c$  search is a part of the physics program of present [27, 28] and several proposed experiments [21]. The theoretical cross section obtained above is consistent with the existing upper limit [28],

$$\sigma(\eta_c) B(\eta_c \rightarrow \gamma\gamma) < 9 nb, \quad (49)$$

if the branching ratio is  $B(\eta_c \rightarrow \gamma\gamma) < 3\%$  as expected. Apart from the total inclusive cross section, we have also calculated the  $p_T$ -distribution of the  $\eta_c$  in our model. The result at  $\theta_{\text{cm}}=90^\circ$  and  $\sqrt{s}=63 \text{ GeV}$  is plotted in Fig. 9 for the two parametrizations, set I and II specified in (B10) and (B11), respectively. We see that  $\eta_c$  and  $\chi$  production is very similar in its  $p_T$

\* Another estimate [26] based on the  $O(\alpha_s^2)$  process, Fig. 1, alone yields for the total cross section,  $\sigma(\eta_c) \sim 6 \mu b$

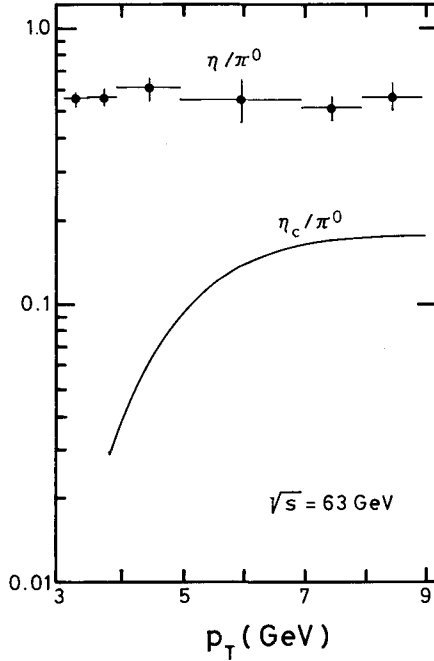


Fig. 10. Predicted  $\eta_c/\pi^0$  ratio at  $y=0$  in comparison to the measured  $\eta/\pi^0$  ratio [30]

dependence and in its absolute yields. The latter are roughly one order of magnitude larger than the  $J/\psi$  yield.

If the model is correct the experimental prospects of detecting the  $\eta_c$  in hadronic reactions are quite promising. Because of the large production rates one can afford a clean decay channel even if its branching ratio is small. Possible modes are:

$$\begin{aligned} \eta_c &\rightarrow \gamma\gamma; & B < 1.3\% \\ &\rightarrow p\bar{p}; & B < 2\% \\ &\rightarrow A\bar{A}; & B < 3\%. \end{aligned} \quad (50)$$

The above branching ratios are experimental limits [29]. Most favoured by experimentalists is the 2 photon channel. The main background in this channel, apart from hadron pairs such as  $\pi^0\pi^0$ , comes from prompt photon pair production via quark-antiquark annihilation,  $q\bar{q} \rightarrow \gamma\gamma$ . However, if the  $\eta_c$  cross section is as big as estimated above, it should be possible to extract a  $\eta_c$ -signal in the two-photon channel [26]. In particular, the larger  $p_T$  the less one should be bothered by the hadronic background. This can be clearly seen in Fig. 10 where we compare the predicted  $\eta_c/\pi^0$  ratio\* to the measured  $\eta/\pi^0$  ratio [30]. Thus, at large  $p_T$  one expects:

$$\eta_c/\pi^0 \sim O(10\%). \quad (51)$$

\* The curve represents the geometric mean of the scaling and non-scaling result of Fig. 9 normalized to the experimental  $\pi^0$ -cross section published recently in [31]

Unfortunately, the absolute yield at  $p_T > 4 \text{ GeV/c}$  looks rather hopeless.

Naturally, together with the  $\eta_c$  also the  $\chi_0$  and  $\chi_2$  states should show up in the  $2\gamma$ -channel. This is because not only the production rates but also the branching ratios into two photons of these 3 states are very similar. More explicitly, one has

$$B_{\gamma\gamma} \sim \frac{\Gamma(\rightarrow \gamma\gamma)}{\Gamma(\rightarrow g g)} = \frac{9}{2} \frac{\alpha^2 e_Q^4}{\alpha_s^2} \sim O(1\%) \quad (52)$$

if one accepts the decay into two gluons as a reasonable approximation of the total decay width of  $^1S_0$  and  $^3P_{0,2}$  resonances.

## VII. Summary

In this paper we have given a fairly detailed and complete account of quarkonium production in a framework which is essentially based on perturbative QCD and the nonrelativistic potential model for heavy quark-antiquark bound states. The dynamics of the bound state production is entirely specified at the level of the short-distance subprocesses.

Unfortunately, our analysis suffers from some uncertainties which are presently unavoidable. One main source are the input parameters:

- (i) normalization of the QCD coupling constant ( $A$ ),
- (ii) quarkonium wave functions ( $R_0, R_1'$ ) and branching ratios ( $^3P_J \rightarrow ^3S_1 \gamma$ ),
- (iii) quark and gluon structure functions,
- (iv) primordial transverse momentum distribution.

Ambiguities also come from the various approximations used:

- (i) nonrelativistic limit,
- (ii) lowest order calculation,
- (iii) Gaussian smearing as a simulation of transverse motion,

and others. Most of these shortcomings are typical for any phenomenological analysis of this kind.

Nevertheless, using reasonable and quite standard values for the input parameters we have achieved a good description of the main features of  $J/\psi$  and  $Y$  production observed in  $pp$  collisions at FNAL/ISR energies. Abundant  $P$ -wave production is another characteristic prediction of the model. We have found consistency with data on  $\chi$  production as far as the spectrum in  $p_T$  is concerned, at least at  $p_T \gtrsim 2 \text{ GeV/c}$ . There exists also experimental evidence from  $\pi p$  collisions at lower energies [32] that

a substantial portion of the  $J/\psi$ 's are actually produced via  $\chi$ -states and their subsequent radiative decays,  $\chi \rightarrow J/\psi \gamma$ . Theoretically, the absolute size of this component depends on the precise value of the derivative of the  $P$ -wave function at the origin.

Particular emphasis has been put on the question of  $\eta_c$  production. We find a  $\eta_c$  cross section at ISR energies, one order of magnitude larger than the  $J/\psi$  cross section. This result let it seem feasible to detect the  $\eta_c$ , and also the  $\chi_0$  and  $\chi_2$  states, through their  $2\gamma$ -decays at low  $p_T$  provided the branching ratios of these states into two photons are not much smaller than 1%. At large  $p_T$ , where the troublesome hadronic background is smallest, the absolute  $\eta_c$  and  $\chi$  yields appear, unfortunately, too low to obtain reasonable statistics.

Furthermore, we have discussed  $\psi'$ ,  $Y'$  and  $Y''$  production and have argued, in particular, that the ratio  $\psi'/\psi$  should be somewhat smaller than what one would naively expect in the absence of  $P$ -wave production. Our theoretical estimates are so far compatible with the measurements. In this respect it is interesting to note that the model predicts a smaller  $\psi'/\psi$  ratio in hadronic collisions than in lepton production because of the impossibility to produce  $P$ -waves via the dominant photon-gluon scattering process,  $\gamma g \rightarrow {}^{2S+1}L_J$  [2]. Such a trend is observed experimentally [9, 22].

One of the most important results of our analysis, we believe, is the demonstration that the relative yields of the various resonances directly reflect properties of the basic QCD cross sections. Since ratios of cross sections are, at the same time, relatively insensitive to the input parameters (except the quarkonium wave functions) the relative rates may provide a crucial test of the short distance dynamics of resonance production.

## Appendix A: QCD-Cross Sections

Here we list the lowest order QCD-cross sections for the resonance production processes investigated in this paper. These cross sections are obtained from the Feynman graphs of Figs. 1–3 as described in Chap. II. We write the formulas in terms of the invariants:

$$\begin{aligned}\hat{s} &= (k_1 + k_2)^2, \\ \hat{t} &= (k_2 - k_3)^2, \\ \hat{u} &= (k_1 - k_3)^2\end{aligned}\tag{A1}$$

where  $\hat{s} + \hat{t} + \hat{u} = P^2 = M^2$  and  $M$  is the mass of the resonance considered. The momenta  $k_i$ ,  $i = 1, 2, 3$  and

$P$  are assigned as indicated in Figs. 1–3. To specify our normalization of the radial wave functions involved we state their relations to familiar decay widths. In lowest order the  $S$ -wave function at the origin,  $R_0$ , is connected to the leptonic  ${}^3S_1$ -width by

$$\Gamma_{\Pi}({}^3S_1) = 4\alpha^2 e_Q^2 R_0^2 / M^2, \tag{A2}$$

whereas the derivative of the  $P$ -wave function at the origin,  $R'_1$ , is related to the gluonic  ${}^3P_0$ -width by

$$\Gamma_{gg}({}^3P_0) = 96\alpha_s^2 R_1'^2 / M^4. \tag{A3}$$

The subprocesses of resonance production can be grouped as follows. To order  $\alpha_s^2$  one only has the *gluon fusion processes*,  $g g \rightarrow {}^{2S+1}L_J$ , of Fig. 1 with the cross sections:

$$\sigma({}^1S_0) = \frac{\pi^2 \alpha_s^2 R_0^2}{3M^3 \hat{s}} \delta\left(1 - \frac{M^2}{\hat{s}}\right), \tag{A4}$$

$$\sigma({}^3P_0) = \frac{12\pi^2 \alpha_s^2 R_1'^2}{M^5 \hat{s}} \delta\left(1 - \frac{M^2}{\hat{s}}\right), \tag{A5}$$

$$\sigma({}^3P_2) = \frac{16\pi^2 \alpha_s^2 R_1'^2}{M^5 \hat{s}} \delta\left(1 - \frac{M^2}{\hat{s}}\right). \tag{A6}$$

To order  $\alpha_s^3$ , on the other hand, one has typically two-by-two scattering processes. The relevant cross sections are given below:

(a)  $g q \rightarrow {}^{2S+1}L_J q$  or  $(q \rightarrow \bar{q})$  (Fig. 2a) with

$$\frac{d\sigma}{d\hat{t}}({}^1S_0) = \frac{2\pi \alpha_s^3 R_0^2}{9M \hat{s}^2} \cdot \frac{(\hat{t} - M^2)^2 - 2\hat{s}\hat{u}}{(-\hat{t})(\hat{t} - M^2)^2}, \tag{A7}$$

$$\frac{d\sigma}{d\hat{t}}({}^3P_0) = \frac{8\pi \alpha_s^3 R_1'^2}{9M^3 \hat{s}^2} \cdot \frac{(\hat{t} - 3M^2)^2 (\hat{s}^2 + \hat{u}^2)}{(-\hat{t})(\hat{t} - M^2)^4}, \tag{A8}$$

$$\frac{d\sigma}{d\hat{t}}({}^3P_1) = \frac{16\pi \alpha_s^3 R_1'^2}{3M^3 \hat{s}^2} \cdot \frac{-\hat{t}(\hat{s}^2 + \hat{u}^2) - 4M^2 \hat{s}\hat{u}}{(\hat{t} - M^2)^4}, \tag{A9}$$

$$\begin{aligned}\frac{d\sigma}{d\hat{t}}({}^3P_2) &= \frac{16\pi \alpha_s^3 R_1'^2}{9M^3 \hat{s}^2} \\ &\cdot \frac{(\hat{t} - M^2)^2 (\hat{t}^2 + 6M^4) - 2\hat{s}\hat{u}(\hat{t}^2 - 6M^2(\hat{t} - M^2))}{(-\hat{t})(\hat{t} - M^2)^4}\end{aligned}\tag{A10}$$

(b)  $q \bar{q} \rightarrow {}^{2S+1}L_J g$  (Fig. 2b) with

$$\frac{d\sigma}{d\hat{t}}({}^{2S+1}L_J) = -\frac{8}{3} \frac{\hat{t}^2}{\hat{s}^2} \cdot \frac{d\sigma}{d\hat{t}}(g q \rightarrow {}^{2S+1}L_J q)|_{\hat{t} \leftrightarrow \hat{s}} \tag{A11}$$

(c)  $g g \rightarrow {}^{2S+1}L_J g$  (Fig. 3) with

$$\begin{aligned}\frac{d\sigma}{d\hat{t}}({}^3S_1) &= \frac{5\pi \alpha_s^3 R_0^2}{9M \hat{s}^2} \cdot \frac{M^2}{(\hat{s} - M^2)^2 (\hat{t} - M^2)^2 (\hat{u} - M^2)^2} \\ &\cdot \{[\hat{s}^2(\hat{s} - M^2)^2] + [\hat{s} \rightarrow \hat{t}] + [\hat{s} \rightarrow \hat{u}]\}\end{aligned}\tag{A12}$$

$$\frac{d\sigma}{dt}(^1S_0) = \frac{\pi \alpha_s^3 R_0^2}{2M\hat{s}^2} \frac{1}{\hat{s}\hat{t}\hat{u}(\hat{s}-M^2)^2(\hat{t}-M^2)^2(\hat{u}-M^2)^2} \cdot \{ [\hat{s}^4(\hat{s}-M^2)^2((\hat{s}-M^2)^2+2M^4) - \frac{4}{3}\hat{s}\hat{t}\hat{u}(\hat{s}^2+\hat{t}^2+\hat{u}^2) \cdot (\hat{s}-M^2)(\hat{t}-M^2)(\hat{u}-M^2) + \frac{16}{3}M^2\hat{s}\hat{t}\hat{u}(\hat{s}^2\hat{t}^2+\hat{s}^2\hat{u}^2+\hat{t}^2\hat{u}^2) + \frac{28}{3}M^4\hat{s}^2\hat{t}^2\hat{u}^2] + [\hat{s} \leftrightarrow \hat{t}] + [\hat{s} \leftrightarrow \hat{u}] \} \quad (\text{A13})$$

The cross sections  $\frac{d\sigma}{dt}(^3P_{0,1,2})$  are not available in a condensed enough form to be given here. They do, however, exist as a somewhat lengthy output of a SCHOONSHIP calculation and are available on request.

## Appendix B: Input Parameters

Here, we summarize the actual values of the various parameters used in our numerical calculations.

### (a) Resonance parameters:

Masses (GeV)

$$^1S_0: \quad \begin{array}{cc} \eta_c & 2.983 \\ \eta'_c & 3.592 \end{array} \quad \begin{array}{cc} \eta_b & 9.0 \\ \eta'_b & 10.0 \end{array} \quad (\text{B1})$$

$$^3S_1: \quad \begin{array}{cc} J/\psi & 3.097 \\ \psi' & 3.685 \end{array} \quad \begin{array}{cc} \Upsilon & 9.46 \\ \Upsilon' & 10.02 \\ \Upsilon'' & 10.30 \end{array} \quad (\text{B2})$$

$$^3P_J: \quad \begin{array}{cc} \chi_0 & 3.414 \\ \chi_1 & 3.507 \\ \chi_2 & 3.551 \end{array} \quad \begin{array}{cc} \chi_{0b} \\ \chi_{1b} \\ \chi_{2b} \end{array} \left. \vphantom{\begin{array}{c} \chi_0 \\ \chi_1 \\ \chi_2 \end{array}} \right\} 9.9 \quad (\text{B3})$$

Leptonic widths (keV)

$$^3S_1: \quad \begin{array}{cc} J/\psi & 4.8 \\ \psi' & 2.0 \end{array} \quad \begin{array}{cc} \Upsilon & 1.2 \\ \Upsilon' & 0.6 \\ \Upsilon'' & 0.4 \end{array} \quad (\text{B4})$$

Branching ratios (%)

$$^3S_1 \rightarrow \mu^+ \mu^-: \quad \begin{array}{cc} J/\psi & 7.4 \\ \psi' & 0.8 \end{array} \quad \begin{array}{cc} \Upsilon & 3.5 \\ \Upsilon' & 1.7 \end{array} \quad (\text{B5})$$

$$^3P_J \rightarrow ^3S_1 \gamma: \quad \begin{array}{cc} \chi_0 & 2.7 \\ \chi_1 & 31.5 \\ \chi_2 & 15.4 \end{array} \quad \begin{array}{cc} \chi_{0b} & 4 \\ \chi_{1b} & 29 \\ \chi_{2b} & 10 \end{array} \quad (\text{B6})$$

Wave functions (GeV<sup>3</sup>)

$$R_0^2: \quad \begin{array}{cc} \text{charmonium} & \text{bottomonium} \\ 1S & 0.49 \\ 2S & 0.29 \\ 3S & 1.79 \end{array} \quad (\text{B7})$$

$$R_1^2/M^2: \quad \begin{array}{cc} 1P & 9.1 \times 10^{-3} \\ & 1.5 \times 10^{-2} \end{array} \quad (\text{B8})$$

### (b) QCD coupling constant:

$$\alpha_s(Q^2) = \frac{12\pi}{(33-2f)\ln\frac{Q^2}{\Lambda^2}} = \begin{cases} 0.41 & Q^2 = M_{J/\psi}^2 \\ 0.28 & Q^2 = M_Y^2 \end{cases} \quad (\text{B9})$$

( $f$  is the number of active flavours,  $\Lambda = 500$  MeV)

### (c) Proton structure functions:

Set I (scaling [16])

$$xG_u(x) = 1.78(1+2.3x)(1-x)^3 \sqrt{x}$$

$$xG_d(x) = 0.993(1-x)^3 \sqrt{x}$$

$$xG_s(x) = 0.21(1-x)^7$$

$$xG_g(x) = 3(1-x)^5 \quad (\text{B10})$$

Set II (scale violating [17])

$$xG_u(x, Q^2) = 2xG_d(x, Q^2) = (2.54 - 0.86s)$$

$$\cdot x^{0.56-0.15s}(1-x)^{2.71+0.81s}$$

$$xG_s(x, Q^2) = (0.99 + 0.72s + 0.96s^2)$$

$$\cdot (1-x)^{8.10-1.49s+5.10s^2}$$

$$xG_g(x, Q^2) = (2.01 - 2.73s + 1.29s^2)$$

$$\cdot x^{-0.93s+0.36s^2}(1-x)^{2.9+1.83s} \quad (\text{B11})$$

with

$$s = \ln \left\{ \frac{\ln \frac{M^2 + p_T^2}{\Lambda^2}}{\ln \frac{Q_0^2}{\Lambda^2}} \right\} \quad \text{and} \quad Q_0^2 = 5 \text{ GeV}^2$$

Note that  $G_u$  and  $G_d$  are valence quark distributions, while  $G_s$  is the full sea quark distribution.

### (d) Primordial $k_T$ -distribution:

$$f(\mathbf{k}_T^2) = \frac{1}{4\pi a^2} e^{-\mathbf{k}_T^2/4a^2}; \quad a = 0.48 \text{ GeV} \quad (\text{B12})$$

## References

1. see e.g., F. Halzen: Production of Heavy Quarks, Proc. XXI. Int. Conf. High Energy Physics, Paris, 1982 and references therein
2. see e.g., R. Rückl, R. Baier: Production of Heavy Quarkonia, Proc. Moriond Workshop New Flavours, Les Arcs, 1982 and references therein
3. M.B. Einhorn, S.D. Ellis: Phys. Rev. **D12**, 2007 (1975); S.D. Ellis, M.B. Einhorn, C. Quigg: Phys. Rev. Lett. **36**, 1263 (1978); C.E. Carlson, R. Suaya: Phys. Rev. **D14**, 3115 (1976); J.H. Kühn: Phys. Lett. **89B**, 385 (1980); Chang Chao-Hsi: Nucl. Phys. **B172**, 425 (1980); R. Baier, R. Rückl: Phys. Lett. **102B**, 364 (1981); Nucl. Phys. **B208**, 381 (1982); J. Finjord et al.: Lapp preprint, LAPP-TH-54 (1982); J. Cleymans, M. Kuroda, G.J. Gounaris: Phys. Lett. **106B**, 143 (1981)

4. R. Barbieri, R. Gatto, R. Kögerler: Phys. Lett. **60B**, 183 (1976); R. Barbieri, R. Gatto, E. Remiddi: Phys. Lett. **61B**, 465 (1976); K. Koller, T. Walsh: Nucl. Phys. **B140**, 449 (1978)
5. A.G. Clark et al.: Nucl. Phys. **B142**, 29 (1978)
6. K. Ueno et al.: Phys. Rev. Lett. **42**, 486 (1979)
7. C. Kourkouvelis et al.: Phys. Lett. **91B**, 481 (1980); I. Stummer: private communication
8. R. Baier, R. Rückl: MPI preprint, MPI-PAE/PTh 58/82 (1982), to be published in Nucl. Phys. B
9. J.J. Aubert et al.: CERN preprint, CERN-EP/82-152 (1982)
10. B. Guberina et al.: Nucl. Phys. **B174**, 317 (1980)
11. J.H. Kühn, J. Kaplan, E.G.O. Safiani: Nucl. Phys. **B157**, 125 (1979)
12. H. Stubbe: Comp. Phys. Comm. **8**, 1 (1974)
13. G. Altarelli, G. Parisi: Nucl. Phys. **B126**, 298 (1977)
14. see e.g., G. Altarelli: Partons in quantum chromodynamics. Phys. Rep. **81**, 1 (1982)
15. H. Krasemann: Z. Phys. C - Particles and Fields **1**, 1989 (1979)
16. G. Altarelli, R.K. Ellis, G. Martinelli: Nucl. Phys. **B157**, 461 (1979)
17. R. Baier, J. Engels, B. Petersson: Z. Phys. C - Particles and Fields **2**, 265 (1979); Z. Phys. C - Particles and Fields **6**, 309 (1980)
18. R.D. Field: Quantum chromodynamics. eds. W. Frazer, F. Henyey. American Institute of Physics 1979, p. 97
19. V. Barger, W.Y. Keung, R.J.N. Phillips: Phys. Lett. **91B**, 253 (1980); Z. Phys. C - Particles and Fields **6**, 169 (1980)
20. Z. Kunszt, E. Pietarinen, E. Reya: Phys. Rev. **D21**, 733 (1980)
21. see e.g.: Proc. SPS-Fixed Target Workshop, CERN, Geneva, 1982
22. H.D. Snyder et al.: Phys. Rev. Lett. **36**, 1415 (1976); B.C. Brown et al.: FERMILAB-PUB-77/54-Exp (1977); J.G. Branson et al.: Phys. Rev. Lett. **38**, 1331 (1977)
23. C. Kourkouvelis et al.: Phys. Lett. **81B**, 405 (1979)
24. J.K. Yoh et al.: Phys. Rev. Lett. **41**, 684 (1978)
25. J.H. Kühn: MPI preprint, MPI-PAE/PTh 32/80 (1980)
26. S. Hemmi: Hiroshima University preprint, HUPD 8101 (1981)
27. C. Kourkouvelis et al.: CERN preprint, CERN-EP/82-108 (1982)
28. R.M. Baltrusaitis et al.: FERMILAB-PUB-79/39-Exp (1980)
29. F. Porter: Proc. 1981 SLAC Summer Institute on Particle Physics, SLAC report N. 245 (1982); T.M. Himel et al.: Phys. Rev. Lett. **45**, 1146 (1980)
30. C. Kourkouvelis et al.: Phys. Lett. **84B**, 277 (1979)
31. E. Anassontzis et al.: CERN preprint, CERN-EP/82-26 (1982)
32. Y. Lemoigne et al.: CERN preprint, CERN-EP/82-15 (1982)